MOLECULAR ENVIRONMENT AND THERMAL X-RAY SPECTROSCOPY OF THE SEMICIRCULAR YOUNG COMPOSITE SUPERNOVA REMNANT 3C 396

The Astrophysical Journal, 727:43 (11pp), 2011 January 20 doi:10.1088/0004-637X/727/1/43

MOLECULAR ENVIRONMENT AND THERMAL X-RAY SPECTROSCOPY OF THE SEMICIRCULAR YOUNG COMPOSITE SUPERNOVA REMNANT 3C 396

Yang Su[1,2], Yang Chen[2,3,7], Ji Yang[1,4], Bon-Chul Koo[5], Xin Zhou[2], Deng-Rong Lu[1], Il-Gyo Jeong[5], and Tracey DeLaney[6]

[1] Purple Mountain Observatory, Chinese Academy of Sciences, Nanjing 210008, China
[2] Department of Astronomy, Nanjing University, Nanjing 210093, China
[3] Key Laboratory of Modern Astronomy and Astrophysics, Nanjing University, Ministry of Education, Nanjing 210093, China
[4] Key Laboratory of Radio Astronomy, Chinese Academy of Sciences, Nanjing 210008, China
[5] Astronomy Program, Department of Physics and Astronomy, Seoul National University, Seoul 151-747, Republic of Korea
[6] Kavli Institute for Astrophysics and Space Research, Massachusetts Institute of Technology, 70 Vassar Street, Cambridge, MA 02139, USA
Received 2010 July 30; accepted 2010 November 8; published 2010 December 30

ABSTRACT

We have investigated the molecular environment of the semicircular composite supernova remnant (SNR) 3C 396 and performed a *Chandra* spatially resolved thermal X-ray spectroscopic study of this young SNR. With our CO millimeter observations, we find that the molecular clouds (MCs) at $V_{\rm LSR} \sim 84$ km s^{-1} can better explain the multiwavelength properties of the remnant than the $V_{\rm LSR} = 67$–72 km s^{-1} MCs that are suggested by Lee et al. At around 84 km s^{-1}, the western boundary of the SNR is perfectly confined by the western molecular wall. The CO emission fades out from west to east, indicating that the eastern region is of low gas density. In particular, an intruding finger/pillar-like MC, which may be shocked at the tip, can well explain the X-ray and radio enhancement in the southwest and some infrared filaments there. The SNR–MC interaction is also favored by the relatively elevated ^{12}CO $J = 2$–$1/J = 1$–0 line ratios in the southwestern "pillar tip" and the molecular patch on the northwestern boundary. The redshifted ^{12}CO ($J = 1$–0 and $J = 2$–1) wings (86–90 km s^{-1}) of an eastern 81 km s^{-1} molecular patch may be the kinematic evidence for shock–MC interaction. We suggest that the 69 km s^{-1} MCs are in the foreground based on H I self-absorption while the 84 km s^{-1} MCs at a distance of 6.2 kpc (the tangent point) are in physical contact with SNR 3C 396. The X-ray spectral analysis suggests an SNR age of ∼3 kyr. The metal enrichment of the X-ray emitting gas in the north and south implies a 13–15 $M_\odot$ B1–B2 progenitor star.

Key words: ISM: individual objects (3C 396 G39.2−0.3) – ISM: molecules – ISM: supernova remnants

Online-only material: color figures

1. INTRODUCTION

The progenitors of core-collapse supernovae are massive stars and they most likely formed in giant molecular clouds (MCs). Because of their short lifetime, one may expect that the supernova remnants (SNRs) of core-collapse supernovae would be near their natal environment. The association with MCs often makes SNRs display irregular morphologies in multiwavelengths, which indicates complicated shock interaction with the complex, inhomogeneous ambient interstellar medium (ISM).

3C 396 (G39.2−0.3) is a semicircular young composite SNR, exhibiting both the central X-ray bright pulsar wind nebula (PWN) and western incomplete half-shell structures in multiwavelengths. In the high dynamic-range Very Large Array (VLA) images of the remnant, a remarkable "tail" extending from the very faint eastern shell of the SNR is revealed and is interpreted as an eastern "blow-out" structure (Patnaik et al. 1990). From VLA 6 and 20 cm data, a large-scale brightness asymmetry is found in the east–west direction across SNR 3C 396, the western half of the remnant having roughly twice the flux density of the east (Anderson & Rudnick 1993). The *Einstein* X-ray emission is bright in the limb and the center of the remnant (Becker & Helfand 1987). Based on *ASCA* X-ray spectral analysis, a nonthermal component in the center of 3C 396 is attributed to a synchrotron PWN (Harrus & Slane 1999). Recently, with about 100 ks high spatial resolution *Chandra* observation, a nonthermal nebula containing a point-like source was also found in the center of the remnant and was interpreted as a synchrotron PWN surrounding a yet undetected pulsar (Olbert et al. 2003). The possibility of the excess microwave emission arising from a spinning dust component toward 3C 396 is investigated at 33 GHz with the Very Small Array (VSA) telescope (Scaife et al. 2007). Based on the detection of H_2 molecules and the sharp southwestern boundary in the radio emission, the remnant is suggested to be encountering an MC in this region (Lee et al. 2009). The remnant is suggested at a distance of about 8.5 kpc because a cavity-like structure of the $V_{\rm LSR} \sim 69$ km s^{-1} molecular gas seems to surround the remnant. The *Spitzer* IRS observation reveals that, along the western shell, the inner [Fe II]-line filament and the outer H_2-line one is found to be spatially separated (Hewitt et al. 2009), which is similar to the result of near-IR 1.64 μm [Fe II] and 2.12 μm H_2 line observations using the Wide-field Infrared Camera aboard the Palomar 5 m Hale telescope (Lee et al. 2009). It is most probably because of the various molecular gas density conditions of the multi-phase preshock ISM across the western shell of 3C 396, where the shock of the remnant is interacting with a complicated distribution of MCs (Hewitt et al. 2009). A detailed investigation of the molecular gas environment and the hot gas interaction with it is thus necessary, which may be helpful to understand the multiwavelength physical properties and the dynamic evolution of this irregularly shaped SNR.

In this paper, we have presented our millimeter CO line observations toward SNR 3C 396 and a spatially resolved *Chandra* thermal X-ray analysis. The observations and the data reduction

[7] Author to whom any correspondence should be addressed.

are described in Section 2. The main observational results and calculations are presented in Section 3. The discussion and conclusions are given in Sections 4 and 5, respectively.

2. OBSERVATIONS AND DATA REDUCTION

The observation was first made in the ^{12}CO(J = 1–0) line (at 115.271 GHz) in 2006 April using the 6 m millimeter-wavelength telescope of the Seoul Radio Astronomy Observatory (SRAO) with single-side band filter and the 1024-channel autocorrelator with 50 MHz bandwidth. The half-power beam size at 115 GHz is 2′ and the typical rms noise level was about 0.2 K at the 0.5 km s^{-1} velocity resolution. The radiation temperature is determined by $T_{\rm R} = T_{\rm A}/(f_{\rm b} \times \eta_{\rm mb})$, where $T_{\rm A}$ is the antenna temperature, $f_{\rm b}$ the beam filling factor (assuming $f_{\rm b} \sim 1$), and $\eta_{\rm mb}$ the main beam efficiency ($\sim$ 75%). We mapped the 14′ × 15′ area covering 3C 396 centered at ($19^{\rm h}04^{\rm m}06^{\rm s}$, 05°27′00″) with grid spacing of $\sim$ 1′.

The follow-up observations were made simultaneously in the ^{12}CO(J = 1–0) line (at 115.271 GHz), ^{13}CO(J = 1–0) line (110.201 GHz), and C^{18}O (J = 1–0) line (109.782 GHz) during 2008 November and December using the 13.7 m millimeter-wavelength telescope of the Purple Mountain Observatory at Delingha (hereafter PMOD). The spectrometer has 1024 channels, with a total bandwidth of 145 MHz (43 MHz) and the velocity resolution of 0.5 km s^{-1} (0.2 km s^{-1}) for ^{12}CO (^{13}CO and C^{18}O). The mean rms noise level of the antenna temperature was less than 0.1 K for those lines. The intensity of the C^{18}O (J = 1–0) emission is too weak to examine its spatial distribution. The half-power beamwidth of the telescope is about 54″ and the main beam efficiency $\eta_{\rm mb}$ was 52%. We mapped the 9′ × 9.′5 area centered at ($19^{\rm h}04^{\rm m}03^{\rm s}$, 05°26′30″) with grid spacing of 30″.

We also made the ^{12}CO(J = 2–1) line observation toward partial regions of the SNR with grid spacing of 30″ in 2010 February using the telescope of the SRAO to complement the data. The half-power beam size at 230 GHz is 48″, the main beam efficiency was $\sim$ 57%, and the typical rms noise level was about 0.2 K at the 0.13 km s^{-1} velocity resolution. The resolution of the SRAO ^{12}CO(J = 2–1) observation and the PMOD ^{12}CO(J = 1–0) observation are very similar, which makes it convenient to directly compare the two observations.

All the CO observation data were reduced using the GILDAS/CLASS package developed by IRAM.[8]

The *Chandra* X-ray and *Spitzer* 24 μm mid-IR observations are also used for analysis. We revisited the *Chandra* ACIS observational data of SNR 3C 396 (ObsIDs: 1988; PI: S. P. Reynolds) with total exposure time of about 100 ks. We reprocessed the event files (from Level 1 to Level 2) using the CIAO3.4 data processing software to remove pixel randomization and to correct for CCD charge-transfer inefficiencies. The overall light curve was examined for possible contamination from a time-variable background. The reduced data, with a net exposure of 93.7 ks, were used for our subsequent analysis. The mid-IR 24 μm observation used here was carried out as the 24 and 70 Micron Survey of the Inner Galactic Disk Program (PID: 20597; PI: S. Carey) with the Multiband Imaging Photometer (MIPS; Rieke et al. 2004). The Post Basic Calibrated Data (PBCD) of the 24 μm mid-IR were obtained directly from the *Spitzer* archive. The VLA 1.4 GHz radio continuum emission (L band) data were adopted from Anderson & Rudnick (1993). The HI-line data and the large-scale ^{13}CO line data were obtained from the archival VLA Galactic Plane Survey (VGPS; Stil et al. 2006) and the Galactic Ring Survey (GRS; Jackson et al. 2006), respectively.

[8] http://www.iram.fr/IRAMFR/GILDAS

3. RESULTS

3.1. Molecular Gas Environment of SNR 3C 396

The large field of view (14′ × 15′) ^{12}CO channel maps are made with the SRAO observation and shown in Figures 1 and 2, overlaid with radio (red thick) and X-ray (cyan thin) contours. The velocity components around 69 km s^{-1} (in 64–72 km s^{-1} interval) and around 84 km s^{-1} (in 80–88 km s^{-1} interval) both seem to have positional correlations with SNR 3C 396. The 69 km s^{-1} MCs are mainly situated north of the remnant (with the 64–67 km s^{-1} molecular gas in the northeast and the 68–71 km s^{-1} gas in the northwest (NW)). The SNR seems to be projected roughly within a cavity-like structure of the ^{12}CO 69 km s^{-1} component (Figure 1). However, the morphology of the 69 km s^{-1} component appears not to match well the radio boundary of the remnant; specifically, the 68–71 km s^{-1} gas appears to overlap the northwestern corner of the remnant. On the other hand, at around 84 km s^{-1} (Figure 2), a thick wall structure of molecular gas is seen in the west; the eastern face of the wall at the 85–87 km s^{-1} interval perfectly follows the western radio boundary of the remnant. The radio contours of the remnant seem to coincide with a cavity at 85–87 km s^{-1}. The CO emission around 84 km s^{-1} and the remnant's radio emission both seem to fade out gradually from west to east.

These characteristics are seen more clearly in the close-up image (Figure 3, left panel) made from the PMOD observation with a higher resolution. As also shown in Figure 3 (left panel), the X-ray/mid-IR/radio emission in the west of the remnant appears to be well confined by the western molecular wall around 84 km s^{-1}. Moreover, a prominent finger/pillar-like MC is seen in the southwest (SW), with one end intruding inside the SNR border. The radio and IR brightness peaks of the remnant are located at the short southwestern section of shell that "cuts" the molecular pillar. Also in the southwestern edge, an X-ray enhancement is coincident with the radio peak; in Section 3.2 below, we will show that this X-ray enhancement is exceptionally soft and of normal metal abundance.

As an attempt to remove the confusion by large-scale density gradient, we used the unsharp masking method as described in Landecker et al. (1999), in which we subtracted the smoothed ^{12}CO intensity map from the original ^{12}CO map. Similar images can also be produced by subtracting the smoothed and scaled ^{13}CO intensity image from the original ^{12}CO image. In the "cleaned" image of the 69 km s^{-1} MCs, the cavity-like structure is seen again (Figure 4, the right panel in the first line), but it clearly does not match well the radio boundary of the remnant. For the 84 km s^{-1} MCs, on the other hand, the southwestern finger/pillar-like intrusion and the western molecular wall can be seen clearer in the "cleaned" image (Figure 4, the right panel in the second line) than in the intensity maps. The western boundary of the SNR appears to perfectly follow the left side of a molecular wall again (Figure 4, the right panel in the third line). A patch of strong ^{12}CO emission around 84 km s^{-1} is seen in the NW, where the radio emission of the SNR is slightly enhanced; this patch can also be discerned in the channel map, Figure 2, at 84 km s^{-1}. In addition, there is another patch of ^{12}CO emission in 87–90 km s^{-1} interval in the eastern "blow-out" region of the remnant (Figure 4, the right panel in the fourth line); it can also be discerned in Figure 2 at 87–88 km s^{-1}.

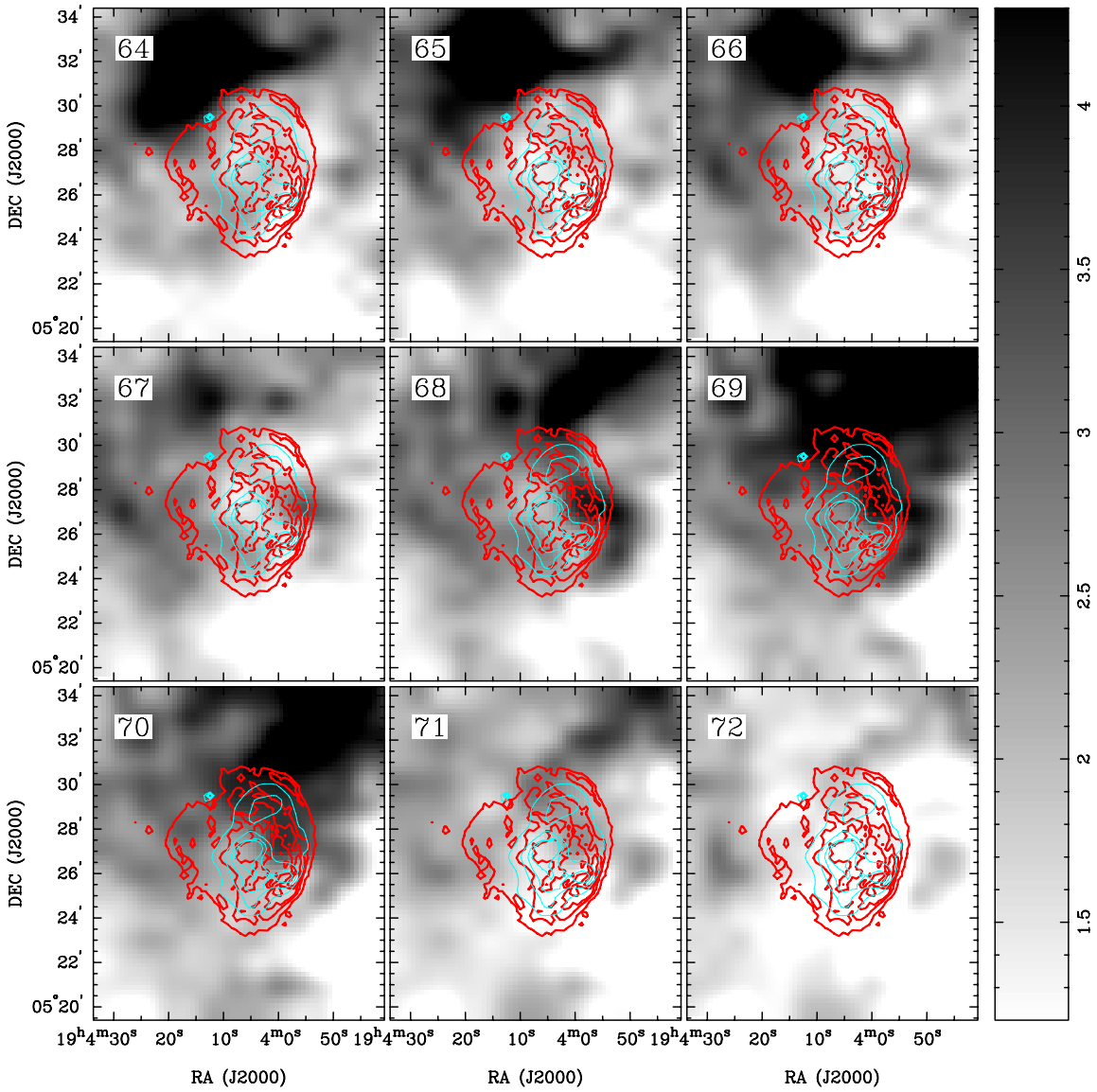

Figure 1. SRAO ^{12}CO ($J = 1$–0) intensity channel maps between 64 and 72 km s^{-1} (smoothed to a resolution of 0.′2 by interpolation), overlaid with the 1.0–7.0 keV X-ray (cyan, thin) contours and the 1.4 GHz radio (red, thick) continuum emission contours at levels of 1.5, 3.5, 5.5, 7.5, 9.5 mJy beam^{-1}.
(A color version of this figure is available in the online journal.)

The integrated CO-line intensity ratio between the different transitions is suggested as a probe of the SNR–MC interaction (Seta et al. 1998; Jiang et al. 2010). The ^{12}CO $J = 2$–$1/J = 1$–0 ratio maps toward 3C 396 at 66.5–68, 68–70.5, 70.5–72, 80–83, 83–85, and 85–88 km s^{-1} (which covers the centers and wings of the 69 and 84 km s^{-1} lines, respectively) are presented in Figure 5. For the ∼84 km s^{-1} component, the ratios are clearly elevated to as high as >0.9 in 80–83 km s^{-1} interval (compared with ∼0.5–0.7 in average) in the southwestern molecular intrusion region and the northwestern molecular patch (corresponding to the two radio brightness peaks, respectively) described above. For the ∼69 km s^{-1} (66.5–72 km s^{-1}) component, although the ratios are weakly elevated in some boundary regions, the ratios are all below 0.9. Therefore the elevated ^{12}CO $J = 2$–$1/J = 1$–0 ratios seem to better imply an interaction of the SNR with the ∼84 km s^{-1} MCs than with the ∼69 km s^{-1} ones.

We have carefully examined the CO spectra in the field of view and presented the ^{12}CO($J = 1$–0), ^{12}CO($J = 2$–1), and ^{13}CO($J = 1$–0) spectra extracted from two regions (in the east and SW, as marked in the right panel in the fourth line of Figure 4) in Figure 6. Around 69 km s^{-1}, the ^{13}CO line profiles are very similar to the ^{12}CO profiles for both the "East" and "SW" regions. Both the ^{12}CO and ^{13}CO spectra of the "SW" region have peaks at 84 km s^{-1}, with broad blue (left) wings in the line profiles. However, it is difficult to judge whether the blue wings of the 84 km s^{-1} ^{12}CO lines are dynamically broadened or not, due to the significant blue wing of the ^{13}CO line and especially a distinct ^{13}CO peak at 81 km s^{-1}. ^{13}CO emission is usually optically thin and indicative of quiescent, intrinsically high-column-density MCs. For the "East" region, both the ^{12}CO and ^{13}CO spectra have peaks at 81 km s^{-1}; notably, there is an additional broadening in the red (right) wing (86–90 km s^{-1}) of the 81 km s^{-1} ^{12}CO line, as compared with little ^{13}CO emission in the same velocity interval. It most likely indicates that the ^{12}CO emission in this interval results from the perturbation suffered by the 81 km s^{-1} molecular gas east of the remnant. Although there is a velocity discrepancy between 81 km s^{-1} for the eastern region and 84 km s^{-1} for the western region, the

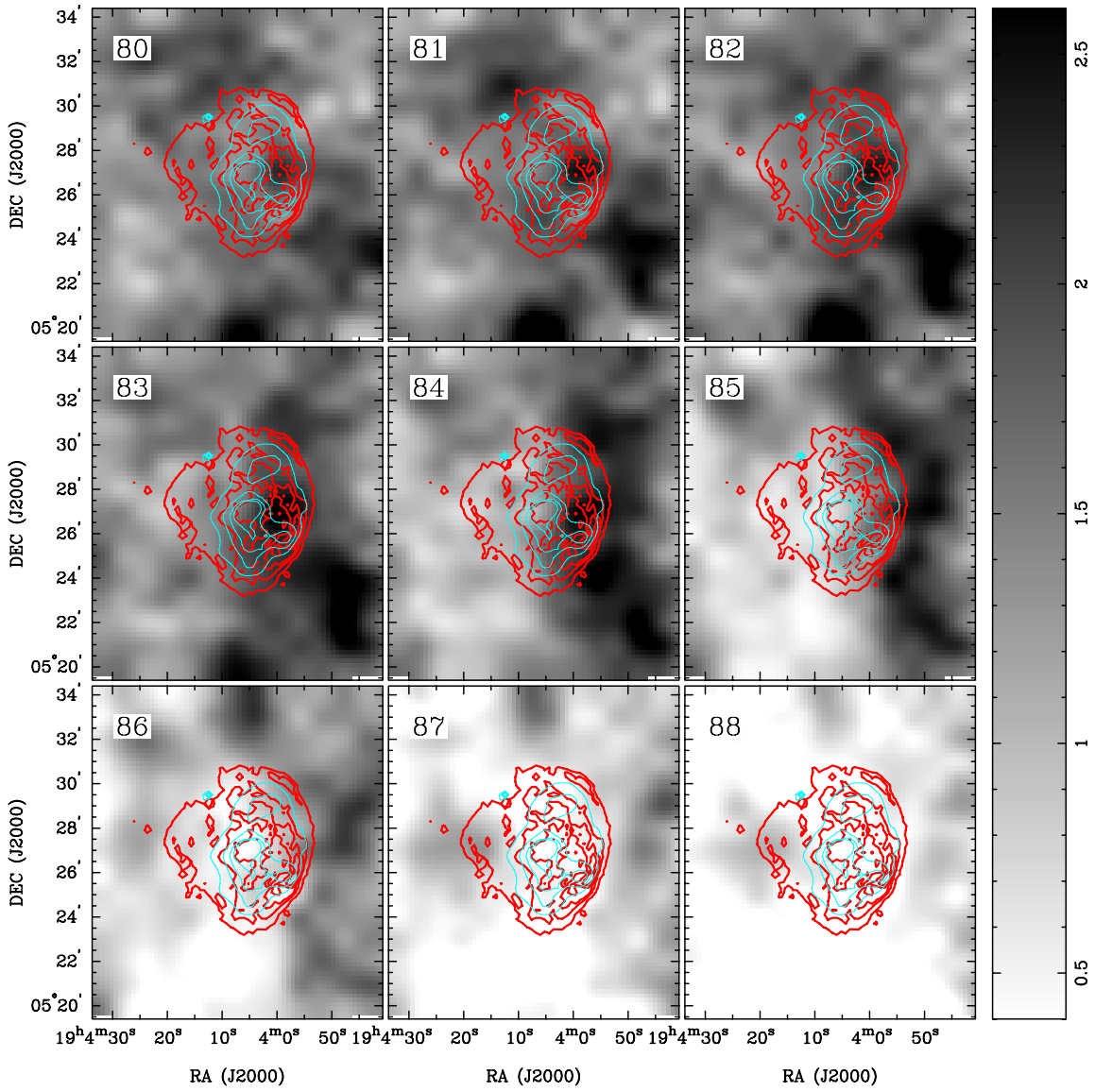

Figure 2. SRAO ^{12}CO ($J = 1$–0) intensity channel maps between 80 and 88 km s^{-1} (smoothed to a resolution of 0.′2 by interpolation), overlaid with the 1.0–7.0 keV X-ray (cyan, thin) contours and the 1.4 GHz radio (red, thick) continuum emission contours at the same levels as in Figure 1.

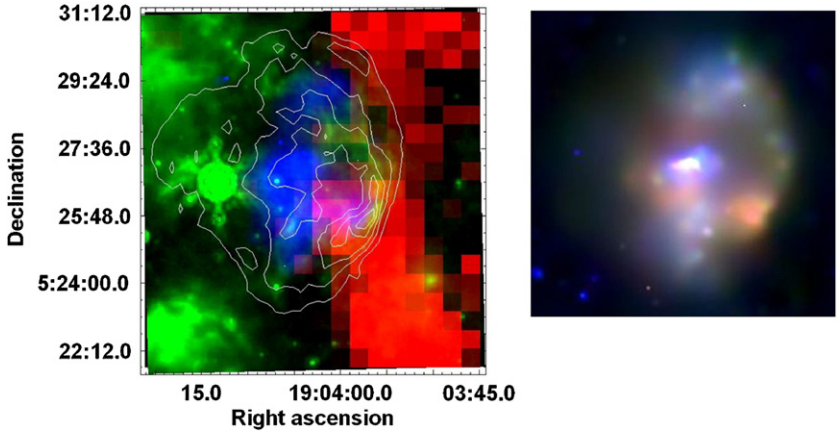

Figure 3. Left: multiband image of SNR 3C 396. The PMOD ^{12}CO intensity map (>2.2 K km s^{-1} or 11σ) in the 85–88 km s^{-1} interval is in red, the *Spitzer* 24 μm mid-IR emission in green, and the *Chandra* 1.0–7.0 keV X-rays (adaptively smoothed with the CIAO program *csmooth* to achieve a S/N ratio of 3) in blue. Each of the intensity maps is in logarithmic scale. The five levels of the VLA 1.4 GHz contours are linear between 78.6% and 12.4% maximum brightness. Right: *Chandra* ACIS X-ray tricolor image of SNR 3C 396. The *Si* (1.65–2.1 keV) is in red, the *S* (2.25–2.6 keV) in green, and the hard continuum (3.0–7.0 keV) in blue.

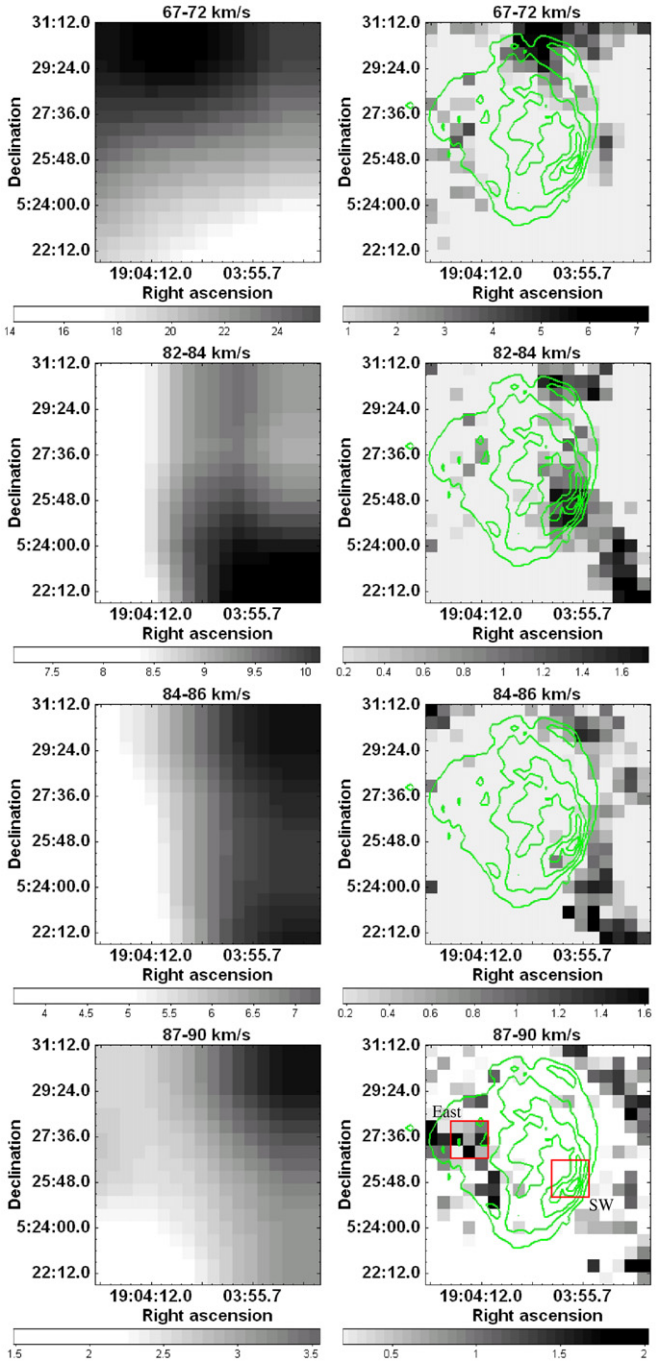

Figure 4. Four left panels: the PMOD ^{12}CO intensity maps in the intervals of 67–72, 82–84, 84–86, and 87–90 km s^{-1}, smoothed to 2′ to illustrate the large-scale confusion in this direction. Four right panels: the PMOD ^{12}CO maps in the same velocity intervals after unsharp masking (see the text in Section 3.1), overlaid by VLA 1.4 GHz contours at the same levels as in Figure 3.

(A color version of this figure is available in the online journal.)

undisturbed clouds in the SNR field may have a wide velocity distribution, e.g., the LSR velocity of MCs with which SNR IC 443 interacts is in the range of −7 to −2 km s^{-1} (van Dishoeck et al. 1993; Hewitt et al. 2006). Thus the 81 km s^{-1} cloud in the east is very likely, together with the 84 km s^{-1} clouds, among the MCs shocked by SNR 3C 396.

The above analysis shows that both the 69 and 84 km s^{-1} molecular components appear to have spatial correlation with SNR 3C 396, but the latter seems to have much better evidence than the former. We will further show that the 69 km s^{-1} clouds are in the foreground of SNR 3C 396, using the VGPS radio and GRS ^{13}CO data.

The 1420 MHz continuum image (Figure 7, upper left panel) displays semicircular brightened structure in the side roughly close to the Galactic plane and faint emission in another side. Following the method used in Tian et al. (2007), we produced the H I spectrum (Figure 7, upper right panel) of the radio peak region of the remnant. The maximum radial velocity of absorption features in the direction toward 3C 396 is up to the tangent point LSR velocity (i.e., ∼ 84 km s^{-1}), and virtually no significant absorption feature appears at negative velocities. It indicates that the distance of SNR 3C 396 is between 6.2 kpc (the tangent point) and 12.5 kpc (the solar circle). Here we have used the rotation curve in Clemens (1985) with $R_0 = 8.0$ kpc (Reid 1993) and $V_0 = 220$ km s^{-1} and adopted the spiral model in Taylor & Cordes (1993; Figure 1 therein).

The H I self-absorption (SA) measurement can provide another clue to the MCs' distances. A single radial velocity indicates two distances (the near and the far kinematic distances) in the inner Galaxy along the line of sight (LOS). MCs in the near distance often display H I SA features and many works have been carried out based on this property (e.g., Liszt et al. 1981; Jackson et al. 2002; Goldsmith & Li 2005; Busfield et al. 2006; Anderson & Bania 2009; Roman-Duval et al. 2009). The H I SA property also seems effective in resolving kinematic distance ambiguity toward SNR–MC associations, such as 3C 397 (Jiang et al. 2010) and CTB 109 (Tian et al. 2010). Figure 7 (lower panels) shows the VGPS H I and GRS ^{13}CO spectra of two regions (as defined in the upper left panel) near the remnant. The H I SA feature is clearly seen at 69 km s^{-1} associated with the ^{13}CO peak, which indicates that the 69 km s^{-1} molecular component is most probably located at the near distance along the LOS, i.e., 4.3 kpc. This component seems to be a part of the 69.65 km s^{-1} MC complex GRSMC G039.34−00.26 at the near side (Roman-Duval et al. 2009), which is apparently outside the distance range 6.2–12.5 kpc inferred for SNR 3C 396.

Therefore, we suggest that SNR 3C 396 is more probably associated with the MCs at ∼84 km s^{-1}. The derived column density and gas mass of some molecular features (the northwestern patch, southwestern pillar and the tip, and the western wall; Figure 8) are presented in Table 1. In the derivation of these parameters, two methods are used and similar results are obtained. In the first method, the H_2 column density is calculated by adopting the mean CO-to-H_2 mass conversion factor $N(H_2)/W(^{12}CO) \approx 1.8 \times 10^{20}$ cm^{-2} K^{-1} km^{-1} s (Dame et al. 2001). In the second method, on the assumption of local thermodynamic equilibrium and the excitation temperature ∼10 K, the ^{13}CO column density is converted to the H_2 column density using the relation $N(H_2) = 7 \times 10^5 N(^{13}CO)$ (Frerking et al. 1982). Assuming a cuboidal volume for the wall region (Figure 8) with size 4.′5 × 4.′5 × 9.′5, the mean molecular density of the western wall is inferred as $\sim 170\, d_{6.2}^{-1} H_2$ cm^{-3}.

3.2. X-ray Properties of 3C 396

Next, we investigate the positional relation of SNR 3C 396's X-ray emission with the CO intensity distribution in detail. In general, we extracted *Chandra* X-ray spectra from five X-ray bright regions (as defined in Figure 9) using the CIAO3.4 script *specextract*. The background spectrum was extracted from four nearby regions (dashed circles in Figure 9). The five onsource spectra were adaptively regrouped to achieve a background-subtracted signal-to-noise ratio (S/N) of 5 per bin.

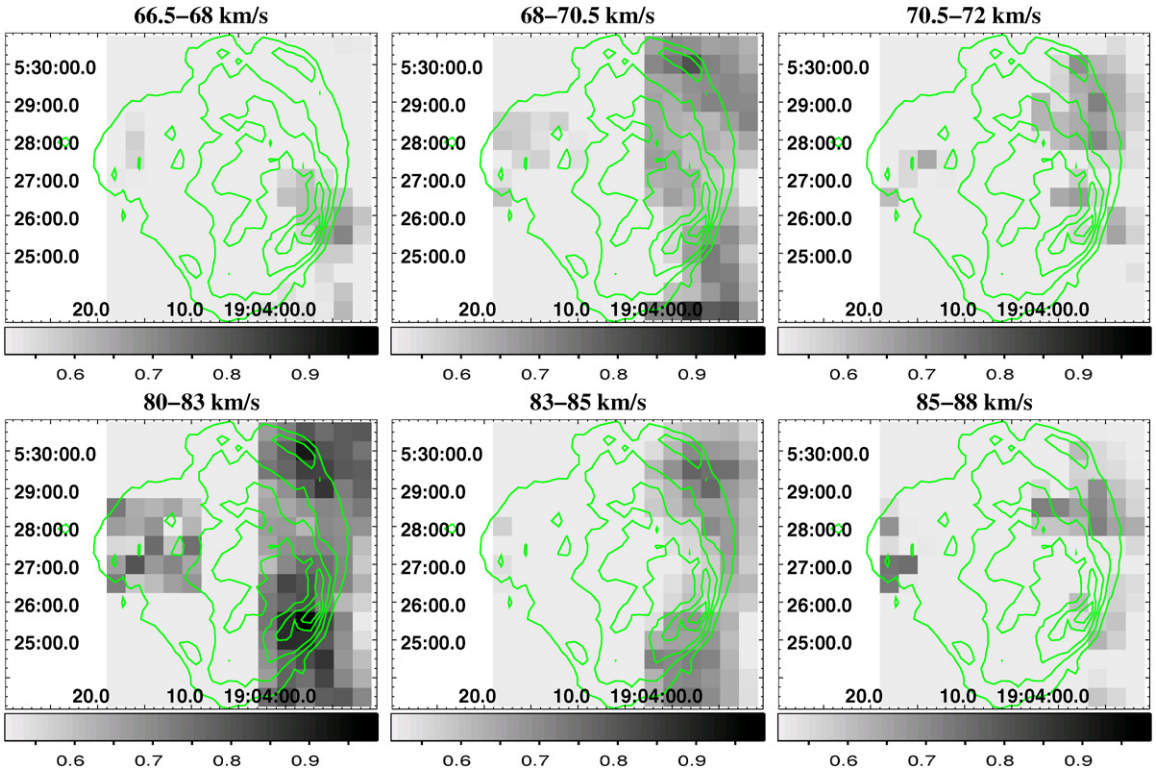

Figure 5. Maps of the ^{12}CO $J = 2$–$1/J = 1$–0 intensity ratio around the SNR 3C 396 at velocity ranges 66.5–68, 68–70.5, 70.5–72, 80–83, 83–85, and 85–88 km s^{-1} after convolving the SRAO ^{12}CO ($J = 2$–1) data to the same beam size as the PMOD ^{12}CO ($J = 1$–0) data. Contours show the VLA 1.4 GHz emission at the same levels as in Figure 3.

(A color version of this figure is available in the online journal.)

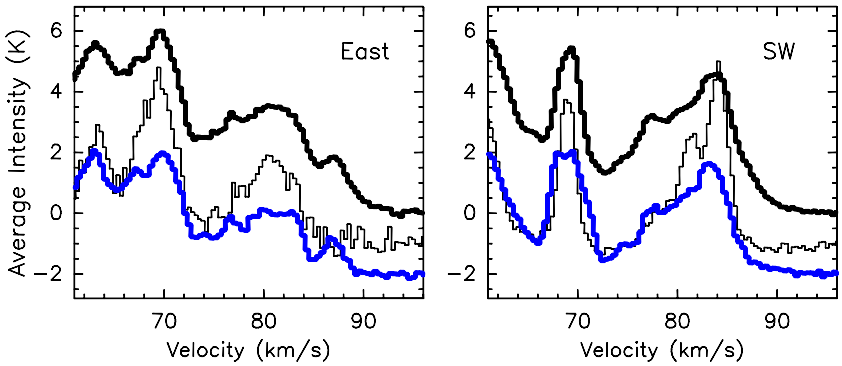

Figure 6. CO spectra in the 61–96 km s^{-1} interval for the eastern (the "East" region in Figure 4, 2.25 arcmin^2 centered at ($19^h04^m14^s$, $05°27'30''$)) and the southwestern (the "SW" region in Figure 4, 2.25 arcmin^2 centered at ($19^h03^m58^s$, $05°25'30''$)) regions of SNR 3C 396. The thick black, thick blue, and thin lines are for the PMOD ^{12}CO ($J = 1$–0), SRAO ^{12}CO ($J = 2$–1), and PMOD ^{13}CO ($J = 1$–0) (multiplied by a factor of 4) emission, respectively. The profiles of ^{13}CO ($J = 1$–0) and ^{12}CO ($J = 2$–1) are shifted by -1 K and -2 K, respectively. The ^{12}CO ($J = 2$–1) spectra are not convolved from beam size $48''$ to the ^{12}CO ($J = 1$–0) beam size $54''$.

(A color version of this figure is available in the online journal.)

Then we used a nonequilibrium ionization (NEI) model to fit the spectra of the remnant. The XSPEC spectral fitting package was used throughout. For the foreground absorption, the cross sections from Morrison & McCammon (1983) were used. The parameters of the fitting are listed in Table 2 with the 90% confidence ranges.

All the five spectra contain distinct lines of Si XIII (∼1.85 keV) and S XV (∼2.45 keV), but the Ar XVII (∼3.12 keV) and Ca XIX (∼3.86 keV) lines are prominent only in the northern and southern regions (Figure 10). The model of our spectral fit generates a variable hydrogen column density from 4.0×10^{22} cm^{-2} to 6.5×10^{22} cm^{-2}. These values are roughly consistent with 4.65×10^{22} cm^{-2} from the diffuse X-ray spectral fitting with *ASCA* X-ray observation (Harrus & Slane 1999) and 5.3×10^{22} cm^{-2} from the entire central nebula spectral fitting with *Chandra* X-ray observation (Olbert et al. 2003). The northern and southern regions have relatively high temperatures ($\gtrsim$1 keV) and slight overabundance of Si, S, and Ca. The temperatures of the other three regions are relatively low, around 0.7 keV. The western edge is also S enriched and, notably, only the southwestern region is found to be of normal abundance. The ionization timescales, $n_e t$, in the northern, southern, and western regions are less than 5.5×10^{11} s cm^{-3} but seems to be higher in the southwestern region ($>4 \times 10^{11}$ s cm^{-3}).

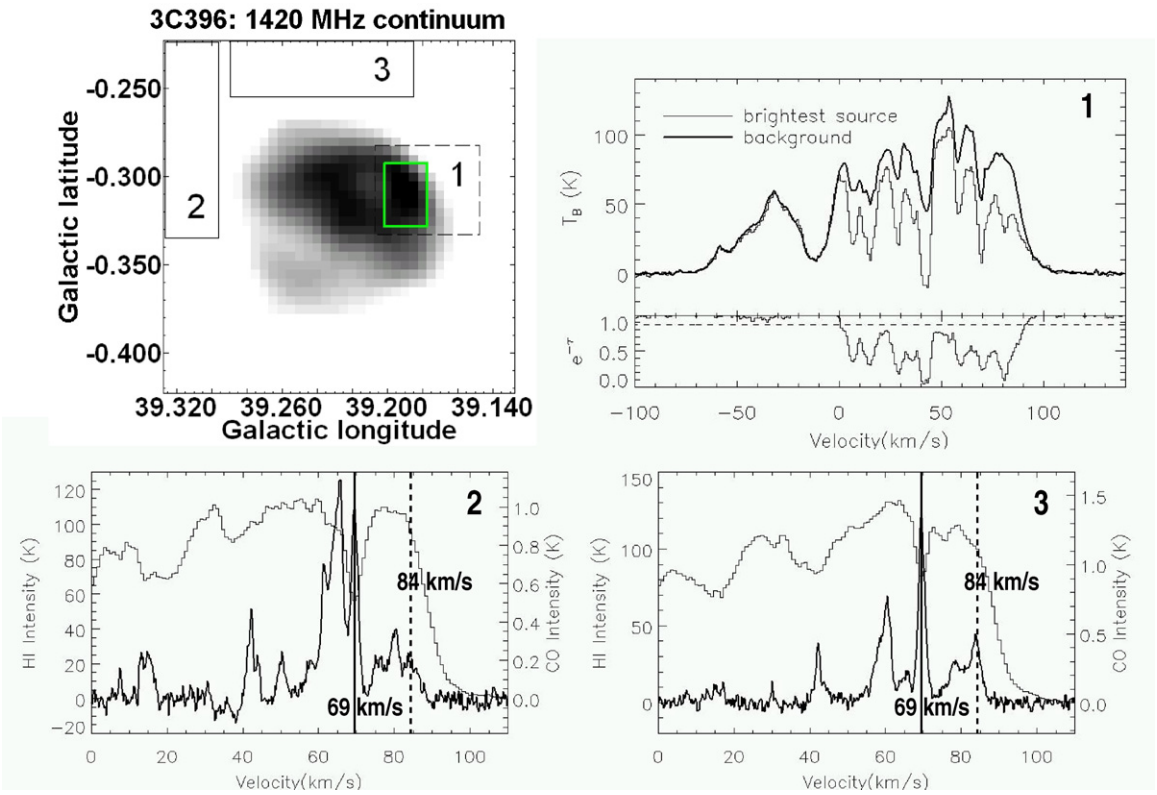

Figure 7. Upper left panel: the VLA 1.4 GHz continuum image of SNR 3C 396. Upper right panel: the H I spectra extracted from box 1. The H I spectrum of the bright source is from the solid-line box area and the background spectrum is from the dashed-line box excluding the solid box area. The dashed line indicates 5σ derivation for velocities $-100\,\mathrm{km\,s^{-1}} \leqslant V_{\rm LSR} \leqslant -50\,\mathrm{km\,s^{-1}}$ and $110\,\mathrm{km\,s^{-1}} \leqslant V_{\rm LSR} \leqslant 140\,\mathrm{km\,s^{-1}}$. Lower panels: the VGPS H I (thin) and GRS ^{13}CO (thick) spectra extracted from boxes 2 and 3 (see the upper left panel), respectively. The vertical solid and dashed lines indicate the position of 69 and 84 km s^{-1}, respectively.
(A color version of this figure is available in the online journal.)

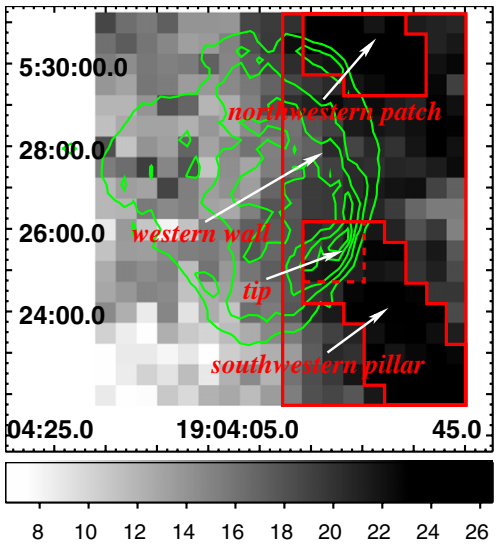

Figure 8. PMOD ^{12}CO intensity map in 82–90 km s^{-1} interval, labeled with the defined regions for the parameter derivation of the 84 km s^{-1} molecular gas. Contours show the 1.4 GHz radio continuum emission toward the remnant at the same levels as in Figure 3.
(A color version of this figure is available in the online journal.)

Table 1
Parameters of the ~84 km s^{-1} Molecular Gas

Region[a]	$N(\mathrm{H_2})(10^{21}\mathrm{cm^{-2}})$[b]	$M(M_\odot)$[b]
Northwestern clump	4.4/4.1	$1.9\times10^3 d_{6.2}^2/1.8\times10^3 d_{6.2}^2$
Pillar	4.6/4.5	$3.7\times10^3 d_{6.2}^2/3.6\times10^3 d_{6.2}^2$
Pillar tip	4.3/4.4	$6.9\times10^2 d_{6.2}^2/7.1\times10^2 d_{6.2}^2$
Western wall	4.2/3.8	$1.3\times10^4 d_{6.2}^2/1.2\times10^4 d_{6.2}^2$

Notes.
[a] Regions are defined in Figure 8.
[b] See the text for the two methods used for the column density derivation.

An estimate of the hot-gas hydrogen-atom density $n_{\rm X}$ of these regions is made using the volume emission measure, $f n_e n_{\rm X} V$, derived from the normalization of the XSPEC model, where n_e is the electron density, V the volume of the emitting region, and f the volume filling factor of the hot-gas ($0 < f < 1$). Here we have assumed $n_e \approx 1.2\,n_{\rm X}$ and oblate spheroids for the defined elliptical regions (Figure 9). The derived physical parameters are listed in Table 3. If we adopt $n_{\rm X} = 2\,f^{-1/2} d_{6.2}^{-1/2}\,\mathrm{cm^{-3}}$ as the mean density of the SNR's hot-gas (where $d_{6.2} = d/6.2\,\mathrm{kpc}$ is used for scaling; Section 4.1) and assume an oblate spheroid ($2\farcm7 \times 3\farcm9 \times 3\farcm9$) for the entire diffuse thermal X-ray emitting volume, $V = 3.0\times10^{58}\,f\,d_{6.2}^3\,\mathrm{cm^3}$, then the mass of the X-ray emitting hot-gas of SNR 3C 396 is $\sim 70\,f^{1/2} d_{6.2}^{5/2}\,M_\odot$.

In the *Chandra* ACIS three-color image (Figure 3, right panel), the X-ray emission is hard in the central PWN region and the northern and southern regions (dominated by the *blue* color), relatively soft along the western boundary (dominated by the *green* color), and softest in the southwestern edge (seen as an *orange* patch). This is consistent with the distribution of hot-gas temperatures derived above. The softest patch is coincident with the tip of the $V_{\rm LSR} \sim 84\,\mathrm{km\,s^{-1}}$ molecular finger/pillar.

Table 2
Chandra X-ray Spectral Fits with 90% Confidence Ranges

Region	N	W	SW	S	E	N+S
$N_{\rm H}(10^{22}$ cm$^{-2})$	$4.84^{+0.30}_{-0.13}$	$5.50^{+0.97}_{-0.92}$	$4.42^{+0.41}_{-0.39}$	$4.74^{+0.26}_{-0.33}$	$4.95^{+1.10}_{-0.83}$	$4.82^{+0.21}_{-0.20}$
$kT_{\rm X}$ (keV)	$1.33^{+0.20}_{-0.19}$	$0.71^{+0.25}_{-0.15}$	$0.66^{+0.10}_{-0.08}$	$1.04^{+0.11}_{-0.14}$	$0.68^{+0.37}_{-0.19}$	$1.21^{+0.13}_{-0.13}$
Si	$1.66^{+0.28}_{-0.27}$	$0.92^{+0.31}_{-0.23}$	$1.23^{+0.23}_{-0.24}$	$1.42^{+0.36}_{-0.27}$	1[a]	$1.56^{+0.21}_{-0.21}$
S	$1.73^{+0.29}_{-0.27}$	$1.99^{+0.77}_{-0.67}$	$1.20^{+0.32}_{-0.28}$	$1.60^{+0.40}_{-0.27}$	1[a]	$1.63^{+0.22}_{-0.21}$
Ca	$1.91^{+1.16}_{-0.86}$	1[a]	1[a]	$3.08^{+1.93}_{-1.45}$	1[a]	$1.98^{+0.93}_{-0.86}$
$\tau(10^{11}$ s cm$^{-3})$	$2.19^{+1.50}_{-0.63}$	$0.42^{+0.46}_{-0.10}$	>4.06	$2.69^{+2.79}_{-1.09}$	>0.84	$2.34^{+1.29}_{-0.74}$
$fn_e n_{\rm X} V/d^2_{6.2}(10^{57}$ cm$^{-3})$	$1.26^{+0.48}_{-0.39}$	$2.73^{+4.32}_{-2.73}$	$2.35^{+1.55}_{-0.88}$	$1.28^{+0.52}_{-0.38}$	$2.34^{+0.63}_{-2.34}$	$2.50^{+0.71}_{-0.52}$
χ^2_r(dof)	1.27(78)	1.21(28)	0.66(48)	1.40(59)	1.14(19)	1.54(101)

Note. [a] Fixed to the solar abundance.

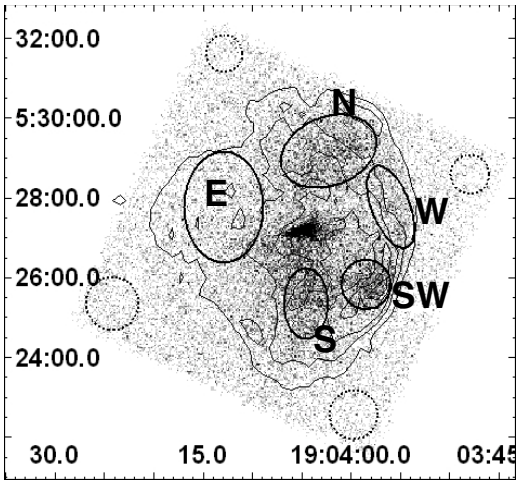

Figure 9. *Chandra* X-ray raw image of SNR 3C 396, labeled with the solid (dotted) defined regions for the source (background) X-ray spectrum extraction. The point sources (except the central pulsar) detected with a wavelet source-detection algorithm have been removed. The contours are the VLA 1.4 GHz radio continuum emission at the same levels as in Figure 3.

Table 3
Parameters of the Hot Gas

Region	N	W	SW	S	E
Volume$(10^{56} f d^3_{6.2}$ cm$^3)$[a,b]	10.1	4.4	1.8	3.5	14.5
$n_{\rm X}$ $(f^{-1/2} d_{6.2}^{-1/2}$ cm$^{-3})$	1.0	2.3	3.3	1.7	1.2
Mass$(f^{1/2} d_{6.2}^{5/2} M_\odot)$	1.2	1.2	0.7	0.7	2.0
IonizationAge $(10^3 f^{1/2} d_{6.2}^{1/2}$ yr)	5.6	0.5	>3.2	4.0	>1.9
Pressure $(10^{-9} f^{-1/2} d_{6.2}^{-1/2}$ dynes cm$^{-2})$	6.1	7.3	9.7	8.1	3.5

Notes.
[a] Here f is the filling factor of the X-ray emitting gas and $d_{6.2}$ is the distance to the remnant in units of 6.2 kpc (Section 4.1).
[b] In the estimate of the volumes, we assume the oblate spheroids for elliptical regions N, W, SW, S, and E, with half axes $0'.88 \times 1'.26 \times 1'.26$, $0'.49 \times 1'.11 \times 1'.11$, $0'.63 \times 0'.63 \times 0'.63$, $0'.59 \times 0'.91 \times 0'.91$, and $1'.01 \times 1'.41 \times 1'.41$, respectively.

4. DISCUSSION

4.1. Association of SNR 3C 396 with the $V_{\rm LSR} \sim 84$ km s^{-1} MCs and the Distance

The cavity-like ^{12}CO structure at $V_{\rm LSR} \sim 69$ km s^{-1} seems consistent with the GRS ^{13}CO data (Lee et al. 2009; Figure 7 therein). Based on such a structure at $V_{\rm LSR} \sim 69$ km s^{-1} that seems to roughly surround SNR 3C 396, Lee et al. (2009) suggest an association of 3C 396 with the ∼69 km s^{-1} MCs and thus adopt a distance 8.5 kpc. However, the H I SA property of the 69 km s^{-1} molecular component indicates that it is most likely to be in the foreground (∼4.3 kpc) toward SNR 3C 396, while the 21 cm H I absorption feature suggests the SNR being located in the distance range 6.2–12.5 kpc (Section 3.1). It thus appears difficult to associate the ∼69 km s^{-1} MCs with the remnant. In our ^{12}CO observation, we indeed find that the cavity-like structure of the 69 km s^{-1} molecular component does not match well the morphology of the remnant (Section 3.1).

Aside from the 69 km s^{-1} MCs, however, we have found that the western boundary of the SNR is perfectly confined by the western molecular wall at $V_{\rm LSR} \sim 84$ km s^{-1} and the multiwavelength (X-ray, mid-IR, and radio) properties are consistent with the presence of the 84 km s^{-1} MCs (Section 3.1).

The eastern ^{12}CO patch (seen in Figure 2, at 87–88 km s^{-1}; Figure 4, the right panel in the fourth line) is shown to have a redshifted broadening (87–90 km s^{-1}) in the ^{12}CO spectral line profiles (Figure 6, left panel) and thus probably represents the molecular gas perturbed by the SNR. The molecular line broadening has been widely used as a kinematic evidence of interaction between SNR shocks and MCs (see Jiang et al. 2010), such as in the studies of prototype interacting SNRs IC 443 (DeNoyer 1979), W28 (Arikawa et al. 1999), HB21 (Byun et al. 2006), and G347.3−0.5 (Moriguchi et al. 2005). More recently, broadened line profiles of optically thin ^{12}CO lines were also successively found in our serial work on SNR–MC interaction (Kes 69, Zhou et al. 2009; Kes 75, Su et al. 2009; and 3C 397, Jiang et al. 2010).

Although the broad blue wings of the ∼84 km s^{-1} ^{12}CO lines of the western region of 3C 396 cannot be exclusively determined to be dynamically broadened profiles (Section 3.1; Figure 6, right panel), the relatively enhanced ^{12}CO $J = 2$–$1/J = 1$–0 ratios in such wings (80–83 km s^{-1}) in the northwestern and southwestern boundaries (Figure 5, lower left panel) coincide with the southwestern molecular intrusion region and the northwestern molecular patch, and also with two radio brightness peaks, respectively, which is in favor of a perturbation of the western molecular gas by the SNR expansion. We note that the maximum ratio obtained here is not higher than 1, while higher values are observed in other interacting SNRs (e.g., W44, IC 443, HB21, G349.7+0.2, and G18.8+0.3; see Dubner et al. 2004 and references therein). Two main reasons may explain why the ratio value in the 80–83 km s^{-1} interval does not exceed unity: (1) the filling factor of the disturbed ^{12}CO ($J = 2$–1) emitting region may be small in the 48″ beam size in 3C 396 compared to that for ^{12}CO ($J = 1$–0), and the line ratios could thus be diluted and (2) the location of 3C 396

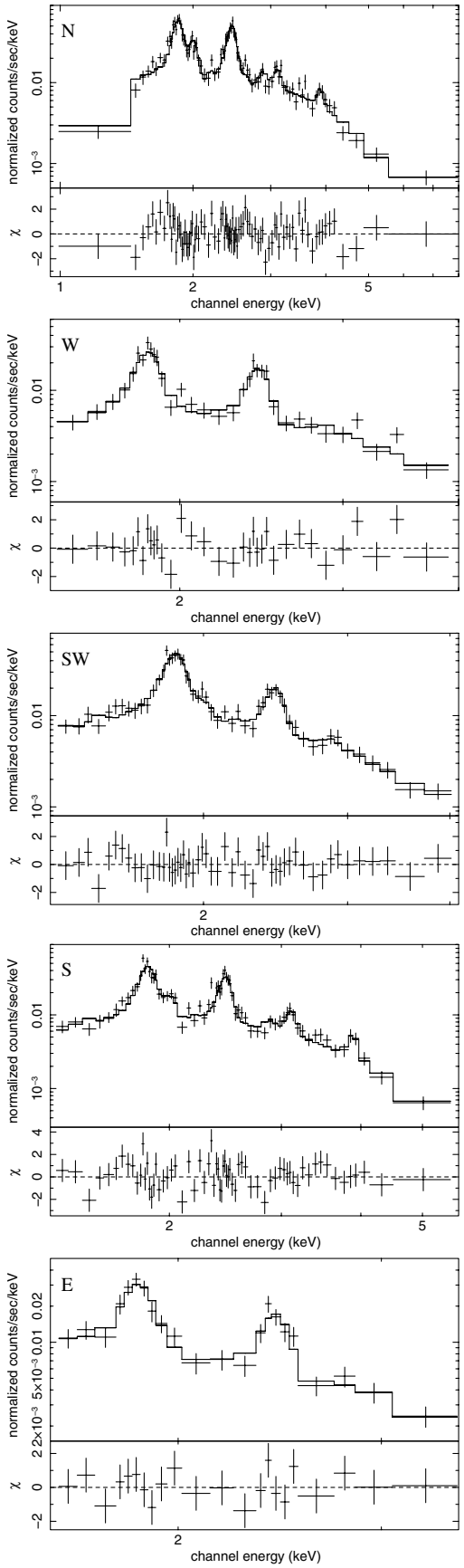

Figure 10. *Chandra* ACIS X-ray spectra of the SNR 3C 396 (taken from a 93.7 ks data), fitted with the *vnei* model.

at the tangent point makes the environment much complicated and may cause unignorable velocity crowding in the interval of interest, with the line wings difficult to differentiate. Actually, e.g., there is a distinct cloud represented by the ^{13}CO line peak at 81 km s^{-1} in the southwestern molecular intrusion region (see Figure 6, right panel). Confusion of the ^{12}CO emission of such gas will decrease the ^{12}CO $J = 2$–$1/J = 1$–0 ratios in the velocity interval.

In multiwavelength morphologies, both the X-ray and radio emissions are bright in the western half and faint in the eastern half (Figures 3 and 9), which is probably because of the large-scale density gradient roughly perpendicular to the Galactic plane. The bright side of the remnant is close to the Galactic plane (see Figure 7, upper left panel, in Galactic coordinates). The bright X-ray, IR and radio emissions in the west are well confined by the thick molecular wall of the ∼84 km s^{-1} component, which may suggest that the SNR expansion is hampered there. This scenario is strengthened by the radio and IR brightness peaks and the soft X-ray patch in the southwestern edge, which are coincident with the "tip" of the intruding finger/pillar of molecular gas. When the SNR shock hits the dense molecular pillar or clumps, it will be decelerated and thus the magnetic field will be compressed and amplified. This can account for the prominent radio enhancement and sharp edge there. Actually, the magnetic field in the SW of the remnant is found to be essentially tangential to the shell, which is probably because the random interstellar magnetic field has been chiefly swept up into the accumulated gas and compressed along with the remnant's shell (Patnaik et al. 1990). (Parenthetically, the tangential field (Patnaik et al. 1990) and the slightly enhanced radio emission in the northwestern edge are consistent with the presence of the dense molecular clump in the NW (Section 3.1).) In X-rays, the low electron temperature, normal metal abundance, and large ionization timescale (as obtained from our spectral fitting) of the soft southwestern X-ray patch can be naturally interpreted by the interaction with the dense molecular pillar. The IR morphology can also be accounted for with the scenario of shock interaction with western molecular gas, as discussed in the following.

In IR, there is a spatial separation between the inner near-IR 1.64 μm [Fe II] and outer 2.12 μm H_2 emission filaments along the western edge of the remnant (Lee et al. 2009; Hewitt et al. 2009). Lee et al. (2009) interprets this morphology due to the SNR shock overtaking the wind of a red supergiant (RSG), giving rise to [Fe II] emission and the interaction with a dense circumstellar bubble, giving rise to H_2 emission. Such an RSG wind bubble 5–7 pc in radius invokes a 25–35 $M_\odot$ progenitor. This mass assumption is different from our estimate of 13–15 $M_\odot$ derived from the X-ray-emitting metal abundances (see below in Section 4.2.3) and is not in agreement with the mass range $\lesssim$25 $M_\odot$ calculated for the neutron star progenitors with metallicity $Z \lesssim Z_\odot$ (Heger et al. 2003). The 13–15 $M_\odot$ progenitor of type-II P supernova (see Section 4.2.3) can only blow an RSG wind bubble of radius $\lesssim$1 pc (Chevalier 2005). However, the spatially separated [Fe II] and H_2 emission can be interpreted in term of SNR–MC interaction. As Reach et al. (2005) and Hewitt et al. (2009) suggest, the H_2 emission can arise from the shock interaction with dense clumps while the [Fe II] emission can arise from the same shock encountering the less dense material at the clumps' surface or from the ejecta.

The bright 24 μm mid-IR emission (Figure 3) may chiefly come from the dust grains and even possibly from the ionic and molecular species in the shocked gas (e.g., Tappe et al. 2006;

Su & Chen 2008) when the western molecular wall is hit by the blast wave. A spinning dust component is invoked to account for the spectral excess at 33 GHz (Scaife et al. 2007), and it seems that the needed dust may lie in the MCs and be heated by the shocked gas.

All these evidences strongly point to a conclusion that SNR 3C 396 is associated, and in physical contact, with the ~84 km s^{-1} MCs. The LSR velocity 84 km s^{-1} corresponds to a Galactic location near the tangent point, at a distance of ~6.2 kpc; this distance is consistent with the range (6.2–12.5 kpc; Section 3.1) inferred from the H I absorption data. We also note that a distance of 6.5 kpc suggested by Hewitt et al. (2009) based on the hydrogen column is very similar to our result. Hereafter, we write the distance to 3C 396 as $d = 6.2\,d_{6.2}$ kpc for scaling.

It was queried by Patnaik et al. (1990) whether the H II complex NRAO 591 (or U39.25 − 0.07), which looks projectively near 3C 396, is associated with the SNR. Since the complex is at $V_{\rm LSR} = 23$ km s^{-1} with the far side distance of 12.1 kpc (Anderson & Bania 2009), it is not associated with the remnant. Instead, it is very likely to be associated with the 22.46 km s^{-1} GRSMC G039.24−00.06 at the far side (Roman-Duval et al. 2009).

4.2. SNR Physics of 3C 396

4.2.1. Global Evolution

According the above multiwavelength analysis, a general scenario for SNR 3C 396 can be established as such: the remnant collides with a molecular wall in the west, flanking a southwestern pillar of molecular gas, and expands in a low-density region in the east (but encountering a clump of backside molecular gas).

The global dynamical evolution of the remnant can be inferred from the X-ray properties. Adopting $kT_{\rm X} \sim 0.9$ keV as the average postshock temperature in the interclump medium, we have the mean blast shock velocity $v_s = [16\,kT_{\rm X}/(3\,\bar{\mu} m_{\rm H})]^{1/2} \sim 8.7 \times 10^2$ km s^{-1}, where $m_{\rm H}$ is the hydrogen atom mass and $\bar{\mu} = 0.61$ is the average atomic weight. Assuming an adiabatic expansion and adopting the SNR radius $r_s \sim 3'.9 \sim 7.0\,d_{6.2}$ pc and the mean density of the interclump medium $n_0 \sim n_{\rm X}/4 \sim 1\,f^{-1/2} d_{6.2}^{-1/2}$ cm^{-3}, the SNR's age is estimated to be $t = (2r_s)/(5v_s) \sim 3\,d_{6.2}$ kyr and the explosion energy is $E = (25/4\xi)(1.4 n_0 m_{\rm H}) v_s^2 r_s^3 \sim 6(n_0/1\,{\rm cm}^{-3}) \times 10^{50} d_{6.2}^{5/2}$ erg (where $\xi = 2.026$). The dynamical age estimated here is consistent with the ionization ages (the time since passage of the shock wave) of the X-ray-emitting gas obtained from the spectral fit (Table 3), except the region "W" for which the ionization age seems relatively low.

4.2.2. Pressure Discrepancy

The thermal pressure of the X-ray-emitting gas is about $p_{\rm h} \sim 1 \times 10^{-8}\,f^{-1/2} d_{6.2}^{-1/2}$ dynes cm^{-2} (Table 3), which is about two order of magnitudes lower than that of the shock ram pressure $p_{\rm cl} \sim 3 \times 10^{-6}$ dynes cm^{-2}, as derived from the H_2 emission of the *Spitzer* IRS observation toward the southwestern region (Hewitt et al. 2009). Similar pressure discrepancies have also been found in the cases of IC 443 (Moorhouse et al. 1991) and 3C 391 (Reach & Rho 1999). Such discrepancies can be explained if the western molecular gas is clumpy and there is a radiative shell between the hot gas and the dense molecular clumps (Chevalier 1999). A radiative shock has been revealed by the *Spitzer* IRS slit observation (Hewitt et al. 2009). On the assumption of a crude pressure balance between the hot gas and the radiative shell, we have (Chevalier 1999)

$$\frac{p_{\rm cl}}{p_{\rm h}} \sim \frac{n_{\rm cl}}{n_0}\left[1 + \left(\frac{n_{\rm cl}}{n_{\rm rs}}\right)^{1/2}\right]^{-2},$$

where $n_{\rm cl}$ is the hydrogen atom density in the clump, n_0 the interclump density, and $n_{\rm rs}$ the density in the radiative shell. The gas density in the dense clump, $n_{\rm cl} \sim 1 \times 10^4$ cm^{-3}, was estimated for the southwestern region from the H_2 lines by two groups of authors (Lee et al. 2009; Hewitt et al. 2009). Considering that the X-ray emission represents the shock interaction with the interclump gas, we may assume n_0 is about 1/4 the density of the hot gas ($n_{\rm X}$; see Table 3) and thus is of order 1 cm^{-3} for the southwestern region. Hence we obtain $n_{\rm rs} \sim 4 \times 10^2$ cm^{-3}. This number is similar to the electronic density (~3×10^2 cm^{-3}) inferred from ionic lines (Hewitt et al. 2009).

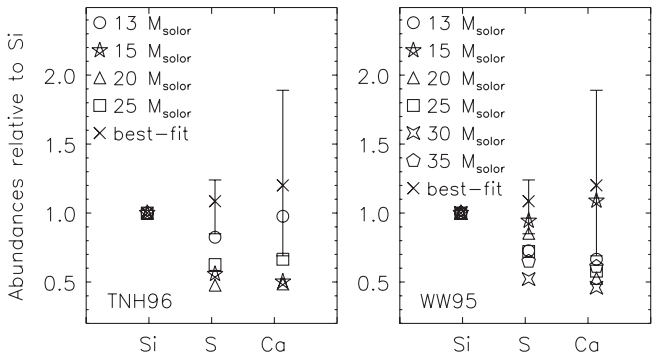

Figure 11. Best-fit abundances of the X-ray emitting gas in the north and south (the "N+S" column in Table 2) relative to Si, compared with the predictions from core-collapsed SN models (TNH96 and WW95).

4.2.3. Supernova Ejecta and Progenitor

In the north and south, the ~84 km s^{-1} CO emission is very weak, the SNR does not seem to encounter the molecular wall, and the X-ray-emitting gas is found to be metal enriched (Table 2). We assume that the observed pattern of metal enrichment can reflect the composition of the supernova ejecta and thus be used to constrain the mass of the progenitor star (following, e.g., Rakowski et al. 2001; Chen et al. 2006). As the presence of a pulsar implies a core-collapse nature of the SN, we plot the relative metal abundances predicted from such SN models for stars with normal metallicities ($Z = Z_\odot$) (Thielemann et al. 1996, hereafter TNH96; Woosley & Weaver 1995, hereafter WW95) in Figure 11. The enrichment appears compatible with the WW95 model for a progenitor mass of $M = 15\,M_\odot$ or the TNH96 model for a progenitor mass of $M = 13\,M_\odot$. A 13–15 $M_\odot$ progenitor is a B1–B2 star (Snow 1982) and ends its life as a type-IIP supernova (Heger et al. 2003).

5. CONCLUSIONS

We have investigated the molecular gas environment of the semicircular young composite SNR 3C 396 in multiple wavelengths, principally with ^{12}CO ($J = 1$–0 and $J = 2$–1) and ^{13}CO ($J = 1$–0) observations in SRAO and PMOD, and performed a *Chandra* spatially resolved thermal X-ray spectroscopic study of the SNR. The main conclusions are summarized as follows.

1. We confirmed a cavity-like structure of molecular gas at ~67–72 km s^{-1} in the 3C 396 SNR region, which was

noticed by Lee et al. (2009) based on the GRS ^{13}CO ($J = 1$–0) data. It is most probably located in the near distance (∼4.3 kpc) according to the H I SA measurement.
2. We find a series of evidence suggesting that the molecular gas at ∼84 km s^{-1} is in physical contact with SNR 3C 396, which can reasonably explain the multiwavelength properties of the remnant. Around this LSR velocity, a molecular wall appears to perfectly confine the western boundary of the SNR, which is bright in X-ray, IR, and radio emission. The CO emission fades out from west to east, indicating that the eastern region is of low gas density, accounting for the radio "blow-out" morphology in the east of the remnant. A molecular pillar is revealed in the SW, with one end intruding inside the SNR border. The shock interaction with this "pillar tip" can explain the X-ray and radio enhancement in the SW and some infrared filaments there. The SNR–MC interaction is also favored by the relatively elevated ^{12}CO $J = 2$–$1/J = 1$–0 line ratios at 80–83 km s^{-1} in the southwestern "tip" and the molecular patch on the northwestern boundary. Redshifted broadening (86–90 km s^{-1}) is detected in the ^{12}CO spectral line profiles of the eastern 81 km s^{-1} molecular patch and may be the kinematic evidence for shock–MC interaction.
3. The establishment of the association between 3C 396 and the 84 km s^{-1} MCs results in a determination of the kinematic distance at ∼6.2 kpc to the remnant, which agrees with a location at the tangent point along the LOS.
4. The diffuse thermal X-ray-emitting gas is found to be metal enriched except in the southwestern X-ray enhancement, and the metal enrichment in the north and south implies that the supernova progenitor is a 13–15 $M_\odot$ B1–B2 star.
5. The X-ray spectral analysis suggests an age of the remnant of ∼3 kyr. There is a pressure discrepancy between the X-ray-emitting gas and the IR emitting cloud shock in the west, which can be explained with the inhomogeneous molecular gas and radiative shells between the hot gas and the dense molecular clumps.

The authors are thankful to the staff members of the SRAO and the Qinghai Radio Observing Station at Delingha for their support in observation and to Lawrence Rudnick for providing the VLA data of SNR 3C 396. We acknowledge the use of the VGPS and GRS data; the National Radio Astronomy Observatory is a facility of the National Science Foundation operated under cooperative agreement by Associated Universities, Inc. This work is supported by the NSFC grants 10621303, 10673003, and 10725312 and the 973 Program grant 2009CB824800.

REFERENCES

Anderson, L. D., & Bania, T. M. 2009, ApJ, 690, 706
Anderson, M. C., & Rudnick, L. 1993, ApJ, 408, 514
Arikawa, Y., Tatematsu, K., Sekimoto, Y., & Takahashi, T. 1999, PASJ, 51, L7
Becker, R. H., & Helfand, D. J. 1987, AJ, 94, 1629
Busfield, A. L., Purcell, C. R., Hoare, M. G., Lumsden, S. L., Moore, T. J. T., & Oudmaijer, R. D. 2006, MNRAS, 366, 1096
Byun, D.-Y., Koo, B.-C., Tatematsu, K., & Sunada, K. 2006, ApJ, 637, 283
Chen, Y., Wang, Q. D., Gotthelf, E. V., Jiang, B., Chu, Y. H., & Gruendl, R. 2006, ApJ, 651, 237
Chevalier, R. A. 1999, ApJ, 511, 798
Chevalier, R. A. 2005, ApJ, 619, 839
Clemens, D. P. 1985, ApJ, 295, 422
Dame, T. M., Hartmann, D., & Thaddeus, P. 2001, ApJ, 547, 792
DeNoyer, L. K. 1979, ApJ, 232, L165
Dubner, G., Giacani, E., Reynoso, E., & Paron, S. 2004, A&A, 426, 201
Frerking, M. A., Langer, W. D., & Wilson, R. W. 1982, ApJ, 262, 590
Goldsmith, P. F., & Li, D. 2005, ApJ, 622, 938
Harrus, I. M., & Slane, P. O. 1999, ApJ, 516, 811
Heger, A., Fryer, C. L., Woosley, S. E., Langer, N., & Hartmann, D. H. 2003, ApJ, 591, 288
Hewitt, J. W., Rho, J., Andersen, M., & Reach, W. T. 2009, ApJ, 694, 1266
Hewitt, J. W., Yusef-Zadeh, F., Wardle, M., Roberts, D. A., & Kassim, N. E. 2006, ApJ, 652, 1288
Jackson, J. M., Bania, T. M., Simon, R., Kolpak, M., Clemens, D. P., & Heyer, M. 2002, ApJ, 566, L81
Jackson, J. M., et al. 2006, ApJS, 163, 145
Jiang, B., Chen, Y., Wang, J. Z., Su, Y., Zhou, X., Safi-Hard, S., & DeLaney, T. 2010, ApJ, 712, 1147
Landecker, T. L., Routledge, D., Reynolds, S. P., Snegal, R. J., Borkowski, K. J., & Seward, F. D. 1999, ApJ, 527, 866
Lee, H.-G., Moon, D.-S., Koo, B.-C., Lee, J.-J., & Matthews, K. 2009, ApJ, 691, 1042
Liszt, H. S., Burton, W. B., & Bania, T. M. 1981, ApJ, 246, 74
Moorhouse, A., Brand, P. W. J. L., Geballe, T. R., & Burton, M. G. 1991, MNRAS, 253, 662
Moriguchi, Y., Tamura, K., Tawara, Y., Sasago, H., Yamaoka, K., Onishi, T., & Fukui, Y. 2005, ApJ, 631, 947
Morrison, R., & McCammon, D. 1983, ApJ, 270, 119
Olbert, C. M., Keohane, J. W., Arnaud, K. A., Dyer, K. K., Reynolds, S. P., & Safi-Harb, S. 2003, ApJ, 592, L45
Patnaik, A. R., Hunt, G. C., Salter, C. J., Shaver, P. A., & Velusamy, T. 1990, A&A, 232, 467
Rakowski, C. E., Hughes, J. P., & Slane, P. 2001, ApJ, 548, 258
Reach, W. T., & Rho, J. 1999, ApJ, 511, 836
Reach, W. T., Rho, J., & Jarrett, T. H. 2005, ApJ, 618, 297
Reid, M. J. 1993, ARA&A, 31, 345
Rieke, G. H., et al. 2004, ApJS, 154, 25
Roman-Duval, J., Jackson, J. M., Heyer, M., Johnson, A., Rathborne, J., Shah, R., & Simon, R. 2009, ApJ, 699, 1153
Scaife, A., et al. 2007, MNRAS, 377, L69
Seta, M., et al. 1998, ApJ, 505, 286
Snow, T. P., Jr. 1982, ApJ, 253, L39
Stil, J. M., et al. 2006, AJ, 132, 1158
Su, Y., & Chen, Y. 2008, Adv. Space Res., 41, 401
Su, Y., Chen, Y., Yang, J., Koo, B.-C., Zhou, X., Jeong, I.-G., & Zhang, C.-G. 2009, ApJ, 694, 376
Tappe, A., Rho, J., & Reach, W. T. 2006, ApJ, 653, 267
Taylor, J. H., & Cordes, J. M. 1993, ApJ, 411, 674
Thielemann, F.-K, Nomoto, K., & Hashimoto, M-A. 1996, ApJ, 460, 408
Tian, W. W., Leahy, D. A., & Li, D. 2010, MNRAS, 404, L1
Tian, W. W., Leahy, D. A., & Wang, Q. D. 2007, A&A, 474, 541
van Dishoeck, E. F., Jansen, D. J., & Phillips, T. G. 1993, A&A, 279, 541
Woosley, S. E., & Weaver, T. A. 1995, ApJS, 101, 181
Zhou, X., Chen, Y., Su, Y., & Yang, J. 2009, ApJ, 691, 516